Hydrides of early transition metals as catalysts and grain growth inhibitors for enhanced reversible hydrogen storage in nanostructured magnesium

Pavel Rizo-Acosta, Fermin Cuevas, Michel Latroche

ARTICLE

Hydrides of early transition metals as catalysts and grain growth inhibitors for enhanced reversible hydrogen storage in nanostructured magnesium

Received 00th January 20xx,
Accepted 00th January 20xx

DOI: 10.1039/x0xx00000x

Pavel Rizo-Acosta, [a] Fermin Cuevas [a] and Michel Latroche [a]

Magnesium is a remarkable hydrogen storage material due to its ability to reversibly absorb high dihydrogen amount at affordable cost. However, its practical use is hampered by the high thermodynamic stability of the hydride and slow reaction kinetics. In this work, one-pot synthesis of nanostructrured magnesium hydride with addition of 5 mol % of Early Transition Metals (*ETM* = Sc, Y, Ti, Zr, V, and Nb) as hydrogenation catalysts is accomplished by mechanochemistry under hydrogen gas. Structural and hydrogenation properties have been systematically analyzed to gain a deep understanding of the influence of *ETM*s on the hydrogenation properties of magnesium. The as-synthetized materials are nanocomposites of MgH_2 and *ETM* hydrides (ScH_2, YH_3, TiH_2, ZrH_2, VH and NbH) with crystallite size of ~ 10 nm. All nanocomposites, but MgH_2-YH_3, have high reversible hydrogen storage (≥ 5 wt.%) at 573 K thanks to catalytic effects induced by *ETM* hydrides leading to fast sorption kinetics. We here demonstrate that, on desorption, *ETM* hydrides can catalyze the recombination of hydrogen atoms. On absorption, formation of coherent interfaces between *ETM* hydrides and MgH_2 favors nucleation of the latter. Moreover, for the peculiar case of TiH_2, lattice mismatch between Mg and TiH_2 hydride limits Mg grain growth, which preserves fast absorption kinetics of MgH_2-TiH_2 nanocomposite on cycling. Thus, the best H-cycling properties are found for MgH_2-TiH_2 nanocomposite with a reversible capacity of 4.8 wt.% after 20 H-cycles and reaction time arbitrarily limited to 15 min.

Introduction

Hydrogen is an attractive alternative to fossil fuels to power mobile and stationary applications. If obtained from renewable sources, hydrogen combined with oxygen produces zero emission of pollutants when used in fuel cells. Moreover, hydrogen is an ideal energy carrier due to its abundance, low-weight and high specific energy (142 MJ/kg)[1]. However, owing to its low volumetric density, compact hydrogen stores are needed to efficiently manage hydrogen production and use. One appealing storage solution, providing high volumetric hydrogen densities (~ 100 kgH_2/m^3) at safe operation conditions of pressure and temperature is hydrogen storage in solids. Magnesium hydride MgH_2, with high gravimetric (7.7 wt. % H_2) and volumetric (109 kgH_2/m^3) storage capacities, is an outstanding candidate for this purpose [2]. Nevertheless, magnesium faces two issues for being used in practical applications. Firstly, hydrogen stored in MgH_2, with a decomposition enthalpy of 75 $kJ/molH_2$, is too stable [3]. Indeed, for feeding fuel cells, magnesium hydride should be heated above 560 K to release hydrogen above 0.1 MPa [4]. Secondly, hydrogenation kinetics of bulk magnesium is extremely slow. For instance, complete hydrogenation of micrometric Mg particles requires a reaction time of several days at the previously given conditions[5]. Reasons for sluggish H-kinetics in Mg are manifold. They are related to both surface and bulk Mg properties. Theoretical calculations show very poor dissociation and recombination of H_2 at Mg surfaces for temperatures lower than 573 K [6]. This is aggravated by the fact that Mg easily forms an oxide passivation layer, even when stored in globe box [7]. As concerns bulk effects, the formation of a core/shell Mg/MgH_2 geometry in combination with the low diffusion coefficient of hydrogen in MgH_2 is often pointed out as the main reason for slow hydrogen absorption in Mg [8–10]. On desorption, there are also significant evidence of kinetic limitations for the nucleation and growth of Mg phase in MgH_2 [11].

To overcome these drawbacks of magnesium as hydrogen store, many strategies have been pursued, such as adding transition metals and their oxides to catalyze hydrogen dissociation and recombination [12–15], alloying Mg with transition metals to weaken Mg–H bonds [16–21], and reducing Mg crystal size to the nanoscale for MgH_2 destabilization and shortening of hydrogen diffusion paths[22,23].

Mechanical milling of magnesium or magnesium hydride with transition metals leads to the formation of nanocomposite (NC) materials with excellent hydrogen sorption kinetics [24–26]. Indeed, reaction kinetics are particularly enhanced by addition of Early Transition Metals (*ETM*)

[a] *Université Paris Est, ICMPE (UMR7182), CNRS, UPEC, F-94320 Thiais, France.*
Electronic Supplementary Information (ESI) available: Rietveld analysis of as-synthetized and H-cycled nanocomposites. Table with molar volumes of ETM hydrides compared to Mg and MgH_2. See DOI: 10.1039/x0xx00000x

belonging to the groups 3 to 5 and periods 4 and 5 of the periodic table; *i.e. ETM* = Sc, Y, Ti, Zr, Y and Nb. All these metals have the ability to form stable hydrides at normal conditions of pressure and temperature [27]. Hydrogen storage properties of nanocomposites NCs made of MgH_2 and *ETM* hydrides are widely reported in the literature [28–33] but comparative studies between them to provide new insights on their role on the sorption properties are still lacking.

In this work, a systematic and comparative study of the hydrogenation properties of MgH_2-*ETM*H_x nanocomposites (*ETM* = Sc, Y, Ti, Zr, V, and Nb) is provided. The atomic ratio Mg:*ETM* has been fixed to 95:5 based on previous publications showing fast reaction kinetics for different systems [34–36]. NCs have been synthetized under identical conditions by reactive ball milling (RBM) under hydrogen atmosphere [21] to get equivalent microstructural properties. Key hydrogenation properties of these NCs (namely H-thermodynamics, H-kinetics and H-cycling) have been determined with the aim to clarify and to gain a better understanding of *ETM* effects on the hydrogenation properties of the Mg-H system.

Experimental

MgH_2-*ETM*H_x nanocomposites were synthetized by RBM of five grams of powder mixtures containing Mg and *ETM* metals (*ETM* = Y, Ti, Zr, V, and Nb). Mg:*ETM* atomic ratio was fixed to 95:5. Origin, particle size and purity (metal basis) of metals are the following: Mg (Alfa Aesar <800 µm, 99.8 %), Y (Stream Chemicals, <400 µm, 99.9 %), Ti (Aldrich, <44 µm, 99.9 %), Zr (Cerac, <44 µm, 99.7%), V (Stream Chemicals, <44µm, 99.5 %), Nb (Chem Pur, <100 µm, 99.9 %). Sc was purchased to China Rare Metals (99.9 %) in the form of millimeter-size lumps. To transform Sc lumps into micrometric powder, Sc was hydrogenated at 473 °C under P_{H2} = 1 MPa. Such ScH_2 powder was used as reactant of RBM process. RBM of 95Mg-5*ETM* powder mixtures under hydrogen gas (6 N Alphagaz) was performed in a high-pressure milling vial (Evicomagnetics, Germany) equipped with both gas pressure and temperature sensors [37]. RBM of additive-free Mg powder was also done for comparison purposes. The commercial vial was connected to a manometric hydrogenation device equipped with calibrated volumes. Using this device, we established the starting hydrogen pressure in the vial (typically 8 MPa) and determined the volume occupied by the gas in the vial (typically 166 cm^3). Monitored vial temperatures were below 59C. The milling process was performed in a Fritsch Pulverisette 4 planetary mill at disk and vial rotation speed of 400 rpm and -800 rpm (relative to disk), respectively, with a ball-to-powder mass ratio of 60:1. Stainless steel balls of 12 mm in diameter were used. Milling was carried out in two cycles, 120 min milling time and 120 min rest each. An experimental procedure described in a previous publication allows for determining the hydrogen uptake with a typical error less than 5% [38]. The samples were fully hydrogenated during the first cycle. Final pressure at this stage is typically 6 MPa. The second cycle, showing no further hydrogen uptake, was used for calibration.

After the RBM, the pressure in the milling vial was released to P_{H2}~ 0.1 MPa and the sample was then recovered in a glove box under argon atmosphere for microstructural analysis and determination of hydrogenation properties. The structural properties of the as-milled NCs were characterized by X-ray diffraction (XRD) with a Bruker D8 Advance diffractometer (Cu $K\alpha_{1,2}$ radiation) in a 2θ range from 25 to 75°. A special airtight sample-holder was used to avoid air exposure. Phase analysis and structural determination of NCs were determined by the full-profile fitting software Fullprof [39] based on Rietveld's method [40,41]. Morphological characterization of NCs was done by Scanning Electron Microscopy (SEM) in back-scattered electron (BSE) mode using a Merlin-Zeiss SEM apparatus. The NCs powders were deposited over a black conducting carbon adhesive tape.

H-Thermodynamic properties of MgH_2-*ETM*H_x nanocomposites were determined through the acquisition of both absorption and desorption Pressure-Composition Isotherms (PCI) at 573 K using a home-made Sieverts' manometric device [42]. Isothermal sorption kinetics measurements were performed at 573 K in the same system at quasi-constant pressure using large reservoirs. NCs were first heated up from room temperature (RT) to 573 K under P_{H2} = 1 MPa to avoid any hydrogen release. Then, isothermal desorption and absorption hydrogenation curves at 573 K were monitored by fixing the sorption pressure to 0.03 and 0.8 MPa, respectively. Those pressures were chosen to provide equivalent driving force for desorption and absorption: $\ln(P_p/P_{des}) = \ln(P_{abs}/P_p) \approx 1.6$, taking into consideration that the equilibrium plateau pressure (P_p) of the Mg/MgH_2 system is 0.16 MPa at 573 K [43]. Sorption time was constrained to 15 min., compatible with the characteristic time needed for refilling hydrogen storage tanks [44]. Sorption curves and the related H-reversible capacities (C_{rev}) were measured over 20 cycles. The structural properties of the cycled NCs were characterized by X-ray diffraction (XRD) and analyzed by the Rietveld's method as described before.

ARTICLE

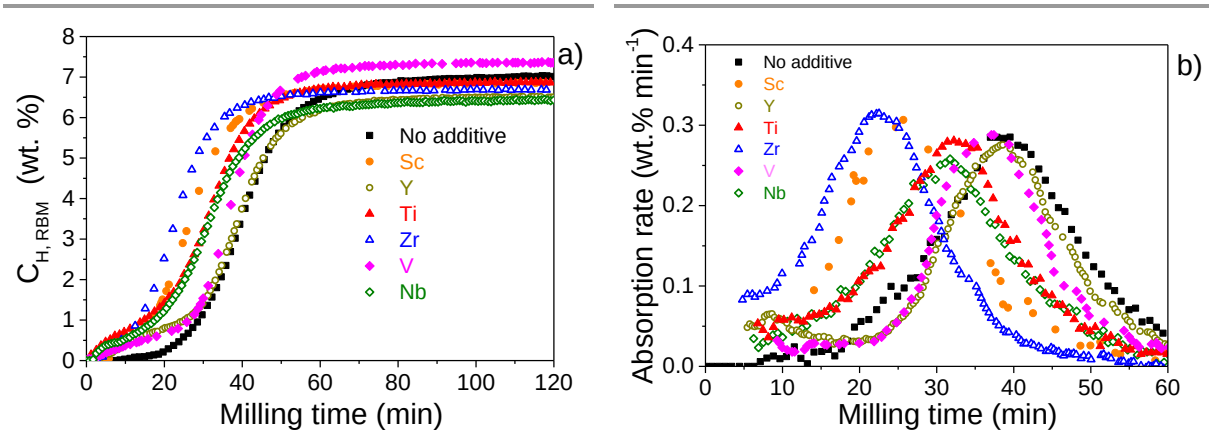

Figure 1. a) Hydrogen uptake curves of 95Mg-5*ETM* powder mixtures during RBM synthesis and b) the corresponding absorption rates (derivative curves of Fig. 1a)

Table 1. Nominal composition, nominal hydrogen content ($C_{H,Nominal}$), measured hydrogen uptake by RBM ($C_{H,RBM}$) and RBM reaction yield of 95MgH_2-5*ETM*H_x nanocomposites. Experimental uncertainties referring to the last digit are given in parenthesis

Additive	Nominal NC Composition	$C_{H,\ Nominal}$ (wt.%)	$C_{H,\ RBM}$ (wt.%)	Yield*(%)
Sc	95MgH_2-5ScH_2	7.4	6.8 (4)	97 (5)
Y	95MgH_2-5YH_3	6.8	6.5 (3)	95 (5)
Ti	95MgH_2-5TiH_2	7.3	6.7 (4)	91 (5)
Zr	95MgH_2-5ZrH_2	6.8	6.9 (4)	102 (5)
V	95MgH_2-5VH_2	7.3	7.3 (4)	100 (5)
Nb	95MgH_2-5NbH_2	6.8	6.4 (3)	94 (5)
No additive	MgH_2	7.6	7.1 (4)	93 (5)

*Reaction yield calculated as 100 $C_{H,RBM}/C_{H,\ Nominal}$. For Sc, the use of ScH_2 as initial reactant is considered.

Results

***Synthesis and microstructural characterization of MgH_2-ETMH_x nanocomposites*.**

Figure 1 shows the hydrogen uptake curves and the corresponding absorption rates during the RBM synthesis of MgH_2-*ETM*H_x nanocomposites as well as for the additive-free MgH_2. In all cases, full reaction takes place in less than 120 min. As gathered in Table 1, the total hydrogen uptake determined by RBM is ≥ 6.4 wt.%, which corresponds to a reaction yield above 90 % considering the expected formation of MgH_2-*ETM*H_x nanocomposites with x = 2 for *ETM* = Sc, Ti, Zr, V, Nb and x = 3 for *ETM* = Y. Indeed, at the used RBM conditions (P_{H2} ~ 8 MPa, T ~ RT) all studied *ETM*s but Y form dihydride compounds. For Y, the formation of YH_3 is reported [27]. The hydrogen uptake curve for additive-free MgH_2 has a sigmoidal shape. When using *ETM* additives, a shoulder is observed at short milling time, $t_m \leq 15$ min, which is assigned to the formation of the *ETM* hydride [28]. At longer milling time, $t_m \geq 15$ min, MgH_2 formation takes place at a rate which depends on the nature of the additive. As displayed in Fig. 1b, the hydrogen absorption rate, which is proportional to the rate of MgH_2 formation, increases along the sequence Y < V < Ti < Nb < Sc < Zr.

Figure 2 displays the XRD patterns of as-milled RBM samples. All patterns exhibit broad diffraction peaks evidencing nanostructured materials with main contribution of the two MgH_2 polymorphs: rutile-type β-MgH_2 (space group, S.G. = $P4_2/mnm$) and orthorhombic γ-MgH_2 (S.G. = *Pbcn*), a metastable high-pressure phase commonly found in grinded MgH_2 [45]. When using *ETM*, additional hydride phases are observed: δ-ScH_2 (S.G. *Fm*-3*m*), ε-YH_3 (S.G. *P*-3*c1*), ε-TiH_2 (S.G. *I4/mmm*), ε-ZrH_2 (S.G. *I4/mmm*), β_2-VH (S.G. *I4/mmm*) [46] and

coexistence of monohydride β-NbH (S.G. *Pnnn*) [47] and dihydride δ-NbH_2 (S.G. *Fm*-3*m*) for *ETM* = Sc, Y, Ti, Zr, V, Nb, respectively. Except for V and Nb, all *ETM*H_x correspond to fully hydrogenated compounds, *i.e.* di-hydride for Sc, Ti and Zr and tri-hydride for Y. In contrast, for V and Nb, mono-hydride phases, instead of fully hydrogenated di-hydride ones, are detected. Indeed, for V and Nb, the equilibrium plateau pressure of the monohydride to dihydride transformation is slightly above atmospheric pressure at room temperature [48]. The plateau pressure is lower for NbH_2 to NbH transformation than for the V case. Thus, since the vial pressure is decreased to atmospheric value before XRD measurements, dihydrides of V and Nb tend to transform (fully for V and partially for Nb) to the monohydride ones.

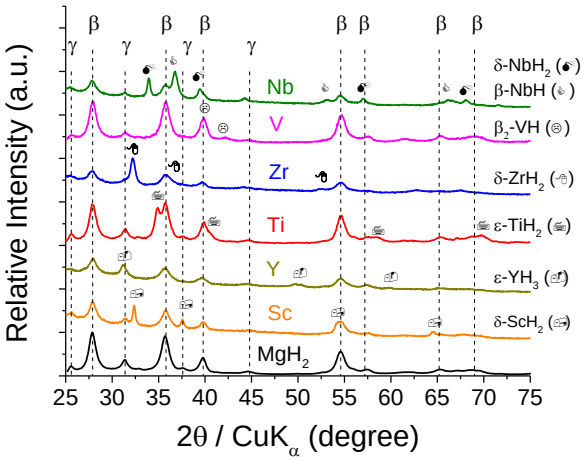

Figure 2. XRD patterns of 95MgH_2+*ETM*H_x nanocomposites after RBM synthesis. Diffraction peaks from β- and γ-MgH_2 phases are marked with vertical lines. Diffraction peaks of *ETM*H_x phases are marked with symbols.

Table 2. Crystallographic data for 95MgH_2-5*ETM*H_x RBM nanocomposites. Detected phases, space group (S.G.), cell parameters, crystallite size (*L*) and Rietveld reliability factors (R_B, R_{wp}) are given. Standard deviations referring to the last digit are given in parenthesis.

Additive	Phase	Content (wt.%)	S.G.	Cell parameters			*L* (nm)	R_B (%)	R_{wp} (%)
				a(Å)	*b*(Å)	*c*(Å)			
Sc	ScH_2	9(1)	*Fm-3m*	4.790(1)	-	-	31(5)	4.4	3.1
	β-MgH_2	69(2)	*P*4_2/*mnm*	4.519(1)	-	3.025(1)	7(1)	8.7	
	γ-MgH_2	22(2)	*Pbcn*	4.535(3)	5.414(3)	4.958(3)	7(1)	1.9	
Y	YH_3	5(1)	*P*-3*c*1	6.366(1)	-	6.646(2)	11(2)	5.9	2.3
	β-MgH_2	68(2)	*P*4_2/*mnm*	4.521(1)	-	3.035(1)	6(1)	2.4	
	γ-MgH_2	27(2)	*Pbcn*	4.571(3)	5.452(3)	4.964(3)	6(1)	5.9	
Ti	ε-TiH_2	10(1)	*I*4/*mmm*	3.173(1)	-	4.403(1)	10(1)	5.7	9.8
	β-MgH_2	69(3)	*P*4_2/*mnm*	4.516(1)	-	3.027(1)	6(1)	2.5	
	γ-MgH_2	21(2)	*Pbcn*	4.528(4)	5.427(4)	4.959(3)	6(1)	9.2	
Zr	ε-ZrH_2	17(1)	*I*4/*mmm*	3.489(1)	-	4.558(2)	10(1)	7.9	4.2
	β-MgH_2	63(2)	*P*4_2/*mnm*	4.542(1)	-	3.028(1)	6(1)	5.1	
	γ-MgH_2	21(2)	*Pbcn*	4.542*	5.422*	4.966*	6(1)	13.4	
V	β_2-VH	7(1)	*I*4/*mmm*	3.039(1)	-	3.390(2)	7(1)	2.5	8.1
	β-MgH_2	80(2)	*P*4_2/*mnm*	4.519(1)	-	3.021(1)	7(1)	3.8	
	γ-MgH_2	13(1)	*Pbcn*	4.540(4)	5.405(5)	4.967(4)	7(1)	6.7	
Nb	δ-NbH_2	7(1)	*Fm-3m*	4.565(1)	-	-	17(2)	3.9	3.3
	β-NbH	10(1)	*Pnnn*	3.457(1)	4.906(1)	4.831(1)	17(2)	2.1	
	β-MgH_2	62(2)	*P*4_2/*mnm*	4.518(1)	-	3.017(1)	7(1)	2.5	
	γ-MgH_2	21(2)	*Pbcn*	4.529(5)	5.423(7)	5.010(5)	7(1)	7.1	
No additive	β-MgH_2	78(2)	*P*4_2/*mnm*	4.526(1)	-	3.027(1)	7(1)	2	8.3
	γ-MgH_2	22(2)	*Pbcn*	4.542(3)	5.422(3)	4.966(3)	7(1)	8	

* Values were fixed to ensure refinement convergence.

All diffraction patterns were analyzed by the Rietveld method [26]. The graphical output is displayed in Fig. S1 (Electronic Supplementary Information, ESI) and crystal data are gathered in Table 2. The cell parameters of the two MgH_2 polymorphs and their relative content (24 ± 3 wt.% of γ-MgH_2) are not significantly affected by *ETM* addition. The former observation suggests that there is no major solubility of *ETM* in the MgH_2 phases. The content of *ETM*H_x phases is ~ 9 wt.% and ~ 17 wt.% for metals of periods 4 and 5, respectively. Considering the different masses of the *ETM*s, this concurs with the nominal atomic ratio of the NCs (*i.e.* 95Mg:5*ETM*); showing additional evidence of no formation of ternary Mg-*ETM*-H phases. The only exception to this general rule is the case of Y, for which only 5 wt.% of YH_3 (instead of nominal 16 wt.%) is detected. This may indicate inhomogeneous distribution of YH_3 (*i.e.* low YH_3 concentration at MgH_2-YH_3 NCs surface) or partial YH_3 amorphization. The crystal size of all detected phases, *L*, determined from the width of diffraction peaks after instrumental correction [26], is in the low nanometric range: ~ 7 nm for MgH_2 phases and comprised between 7 and 17 nm for *ETM*H_x phases. The crystal size for ScH_2 is significantly larger (31 ± 5 nm), which may result from the different preparation route for this hydride.

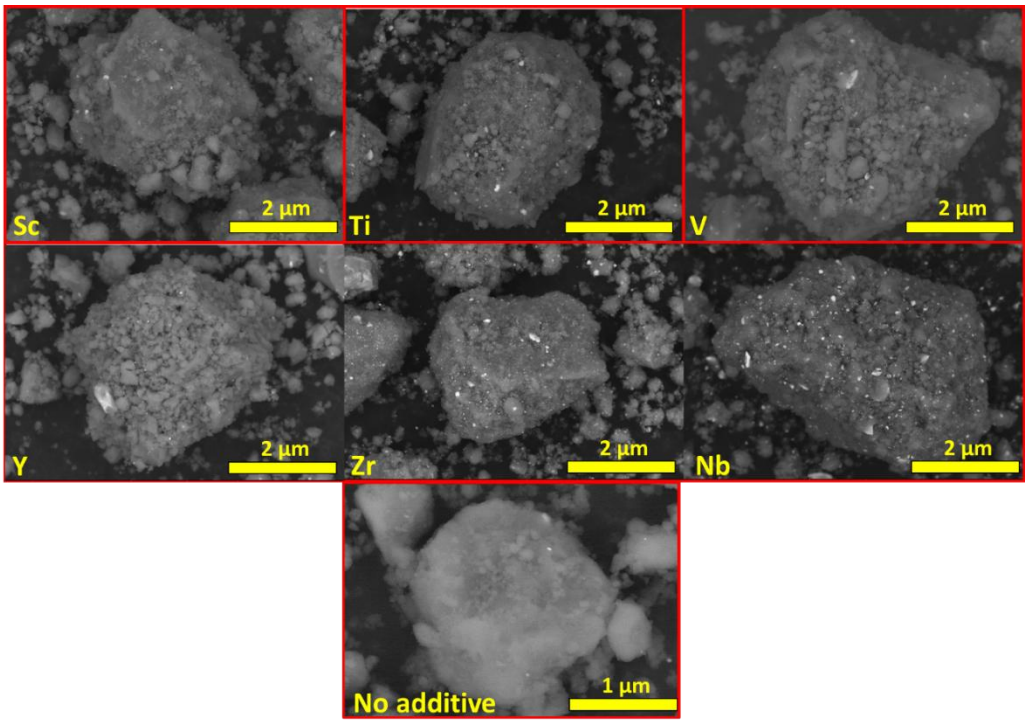

Figure 3. SEM images in BSE mode of hydrogenated MgH_2-*ETM*H_x powders after RBM synthesis

SEM images in BSE mode of as-synthesized MgH_2-*ETM*H_x NCs, as well as for the MgH_2 sample without additive, are shown in Figure 3. All samples consist of micrometric agglomerates (size ~ 2 µm) formed by ~ 20 nm in size primary particles. Homogeneously distributed tiny white dots are observed in all SEM images. These white dots reveal the presence of phases with higher electronic density as compared to the main constituent MgH_2. They are clearly observed for Ti, Zr, V and Nb and in less extent for Sc and Y. They are assigned to the corresponding *ETM*H_x hydrides. These hydrides are homogenously dispersed all over the MgH_2 matrix in agreement with previous RBM studies performed for the MgH_2-TiH_2 system [49,50].

Hydrogen sorption properties.

H-Thermodynamics. PCI measurements at 573 K within the pressure range 10^{-2} to 1 MPa were carried out for all NCs and are shown in Figure 4. Both absorption (Fig. 4a) and desorption (Fig. 4b) data show flat plateau pressures P_P at values close to those reported for the binary Mg-H system. Therefore, thermodynamic properties of the Mg-H system are not significantly modified by the presence of *ETM*H_x hydrides. At low pressure, $P_{H2} \leq 0.01$ MPa, a low hydrogen amount, between 0.3 and 0.5 wt.%, is trapped in the NCs. It is attributed to irreversible hydrogen stored in *ETM*H_x hydrides. At the measured conditions, Sc, Ti and Zr form stable di-hydride phases, Y forms tri-hydride YH_3, while hydrogen content in VH_x and NbH_x phases slightly varies between x ~ 0.3 and 0.8 [28]. YH_3 decomposes into YH_2 at ~0.01 MPa [51].

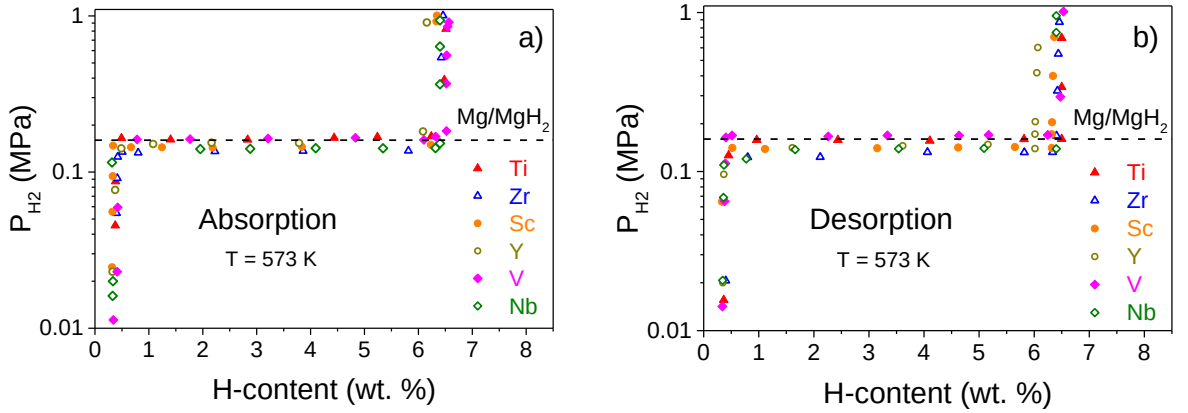

Figure 4. PCI curves at 573 K of MgH_2-*ETM*H_x NCs. a) absorption, b) desorption. Expected plateau pressure for Mg/MgH_2 transformation, $P_{P\ (573\ K)}$ = 0.16 MPa, is depicted by a dashed line.

Hydrogen kinetics and cycling. Figure 5 shows the hydrogen sorption curves at 573 K of MgH_2-*ETM*H_x NCs and their evolution on cycling for selected sorption sweeps. The RBM synthesis is considered as the first absorption reaction. Within the studied pressure window (P_{H2}(abs) = 0.8 MPa, P_{H2}(des) = 0.03 MPa), H-sorption curves refer to the reversible MgH_2/Mg transformation as derived from PCI data (Fig. 4).

Desorption curves for all NCs are essentially linear at short reaction time. On the first cycle, desorption rates increase as Y < Sc < Ti < Zr ~ Nb ~ V. Yttrium additive hardly accelerates desorption kinetics of MgH_2. Desorption rate for Y is 0.06 wt.% min^{-1} leading to 1 wt% of hydrogen release after 15 min. At the opposite, V additive provides the fastest kinetics with initial desorption rate of 3 wt.% min^{-1} and total hydrogen release after 15 min of reaction of 6.1 wt%, which represents 90% of the hydrogen stored in the MgH_2 counterpart of the MgH_2-VH nanocomposite. The 2nd desorption sweep displays similar features, except for Sc and Ti curves which have faster kinetics as compared to the 1st desorption sweep. This enhancement is particularly significant for Ti additive, with initial desorption rate of 3 wt.% min^{-1} and total H-release of 5.2 wt.%. These trends are confirmed on further cycling (see desorption sweep at the 20th cycle) with enhanced rates for Sc, while Ti, Zr, Nb and V additives provide fast and similar kinetics. For additives of groups 4 and 5, the total hydrogen release at cycle 20 is attained in less than 5 min. In addition, it is worth noting that for Ti the total hydrogen release is rather stable on cycling (5.2 and 4.8 wt.% at cycles 2 and 20) whereas it decreases significantly for Zr, Nb and V additives.

Absorption curves for all NCs follow deceleratory functions which are typical of diffusion-controlled reactions [52]. Reaction rate for Y is sluggish as for desorption. It improves to a certain extent for Sc and much more for *ETM*s of groups 4 and 5 whose absorption curves deserve detailed description. For these NCs, very fast absorption rates (over 10 wt.% min^{-1}) are monitored in the 2nd sweep at short reaction time, followed by a drastic slowing down of kinetics at long reaction time. Indeed, absorption curves can be described as a two-step reaction process with fast (first step) and slow (second step) reaction kinetics. The relative contributions of these two steps changes on cycling. Taking *ETM*s = Zr as an example, it absorbs at the 2nd cycle 4.8 and 0.2 wt% within the first and next 14 minutes, respectively, whereas, at the 20th cycle, it absorbs 2.5 and 0.9 wt% under the same periods of time. Thus, for *ETM*s of groups 4 and 5, the extent of the Mg to MgH_2 reacted fraction that quickly absorbs hydrogen within the first step gradually decreases on cycling, while that of the second step, with slower kinetics, increases on cycling. Interestingly, this evolution is less pronounced for *ETM*s = Ti, whose absorption kinetics remain rather stable on cycling. As a final remark, hydrogen uptake in a given cycle is observed to be slightly but systematically lower than hydrogen release in the previous one. This indicates that the absorption sweep is limiting as compared to the desorption one.

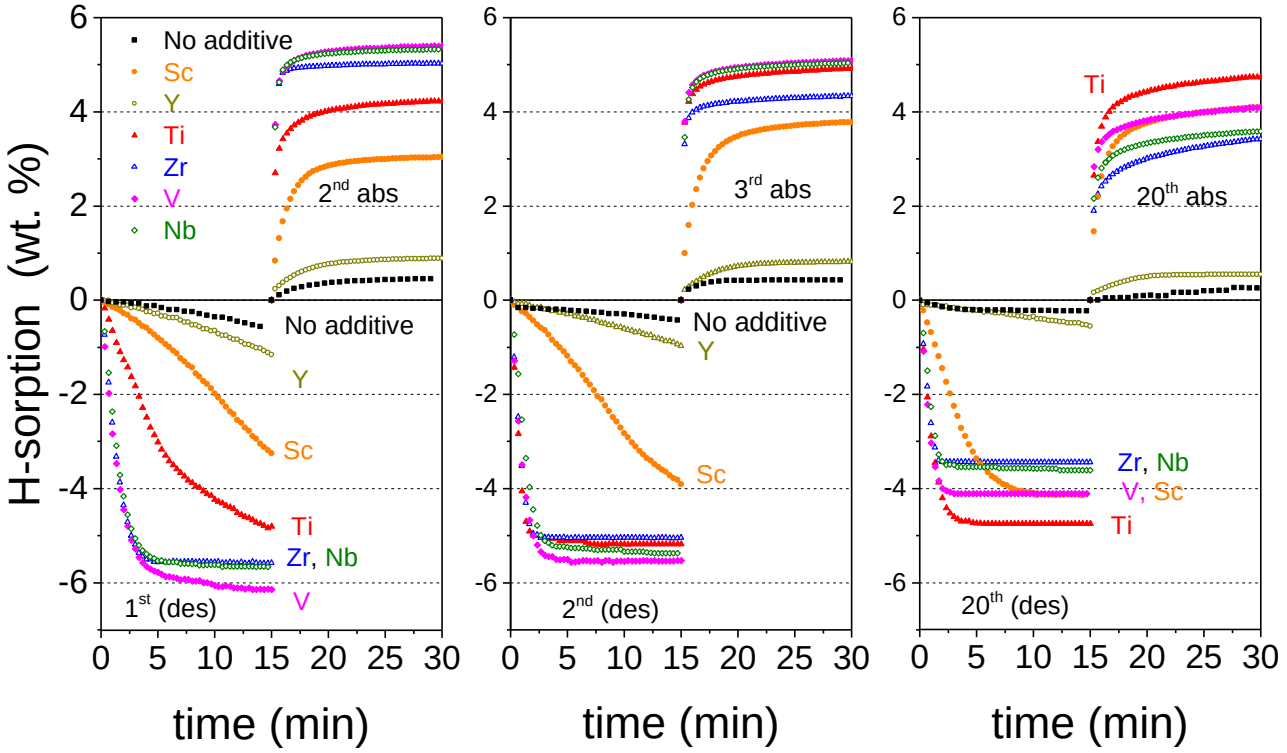

Figure 5. Hydrogen sorption curves at 573 K of MgH_2-*ETM*H_x NCs for different sorption sweeps. Absorption and desorption hydrogen pressures fixed to 0.8 and 0.03 MPa, respectively. Sorption time limited to 15 min.

For each hydrogenation cycle, the reversible hydrogen capacity C_{rev} of MgH_2-*ETM*H_x NCs has been determined from the cycling sorption curves (Figure 5) and is depicted in Figure 6. Four different trends can be distinguished. For Y, the reversible capacity is very low (1 wt.%) from the first cycle, being only slightly better than additive-free MgH_2 (0.6 wt.%). It results from the very sluggish reaction kinetics on desorption for both materials. For Sc, an activation-like behavior is observed. It starts at low C_{rev} (3.2 wt.%), increases up to a maximum (4.8 wt.%) after 7 cycles and then gradually decreases down (4.1 wt.%) upon long-cycling. This activation feature results from the enhancement of desorption kinetics for Sc on cycling (Figure 5). For Zr-, Nb- and V-containing NCs, high C_{rev} (between 5.6 and 6.1 wt.%) are obtained at the first cycle but gradually decrease on cycling (between 3.5 and 4.1 wt% at cycle 20). This decay is assigned to the slowing down of absorption kinetics on cycling for these NCs. Finally, Ti provides the most stable cycling behavior with the best reversible capacity (4.8 wt.%) remaining stable upon 20 cycles. This performance results from fast desorption kinetics as well as stable absorption kinetics on cycling.

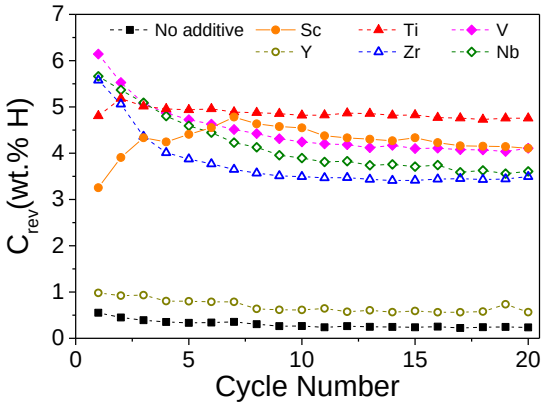

Figure 6. Evolution of the reversible capacity on cycling of MgH_2-*ETM*H_x nanocomposites

Discussion

In most cases, formation of MgH_2 by RBM is accelerated by the presence of *ETM* additives (Fig. 1). This enhancement can be assigned either to surface effects, *i.e.* catalytic dissociation of hydrogen molecules at the surface of *ETM*H_x nanoparticles, or to bulk effects such as favoured MgH_2 nucleation at Mg/*ETM*H_x interfaces. Yttrium, which is hydrogenated as YH_3 in the early state of milling, is an exception to this general rule. MgH_2 rate formation during RBM is poorly affected by YH_3. The origin of this will be later discussed when analysing the hydrogen properties of MgH_2-YH_3 nanocomposite.

Whatever the *ETM* used, microstructural properties of the as-synthetized materials are very similar. They form two-phase nanocomposites made of MgH_2 and *ETM*H_x. In all cases, MgH_2 crystallizes with the coexistence of β-rutile and γ-metastable polymorphic forms in weight ratio 76:24 wt% and crystallite size of ~ 7 nm (Table 2). Moreover, MgH_2-*ETM*H_x nanocomposites form micrometric agglomerates ~ 2 μm in size (Fig.3). Such microstructural properties are typical for MgH_2 materials synthetized by mechanochemistry of Mg under hydrogen atmosphere as well as by mechanical milling of MgH_2 under argon [53].

The thermodynamic properties of the Mg-H system at 573 K are not modified in RBM nanocomposites by the presence of *ETM*H_x phases (Fig. 4). Indeed, the crystallite size of MgH_2 is too large and MgH_2/*ETM*H_x interface-energy contribution is too low to give rise to any significant thermodynamic change in the Mg-H_2 solid-gas reaction [22,30,54,55]. It is worth noting that formation of ternary Mg-*ETM*-H phases has not been detected. If that had happened, thermodynamic modifications would have been observed as it occurs for Mg-based complex hydrides incorporating late transition metals (*e.g.* Mg_2NiH_4) [56]. Although the microstructural properties of all nanocomposites are alike, and the thermodynamic properties of the Mg-H system are not modified by the presence of *ETM*H_x, the H-kinetics (Fig. 5) and H-cycling (Fig. 6) properties of MgH_2-*ETM*H_x nanocomposites strongly depend on the nature of the additive. In other words, the *ETM*s do play a key role in the transport of hydrogen in MgH_2-*ETM*H_x nanocomposites but not in thermodynamics.

To gain a better understanding on the additive role, as displayed in Figure 7, the hydrogen content in the nanocomposites after each sorption sweep was evaluated and assigned to each phase. The initial H-content was fixed to the nominal capacity of the nanocomposite (Table 1) and then, desorbed and absorbed hydrogen amounts at each cycle sweep (Fig. 5) were considered to determine H-contents. This allows to estimate the amount of retained MgH_2 (*i.e.* non-desorbed magnesium hydride) at the end of desorption sweeps as well as the amount of unreacted Mg (*i.e.* non-hydrogenated Mg) for absorption ones (respectively top and bottom hatched areas in Figure 7). The irreversible hydrogen content stored in the form of thermodynamically stable *ETM*H_x phases (grey area at bottom of Fig. 7) is also represented. In this way, the white area located between the upper and lower hatched ones gives a clear picture of the available reversible capacity C_{rev} for the MgH_2-*ETM*H_x nanocomposites upon cycling.

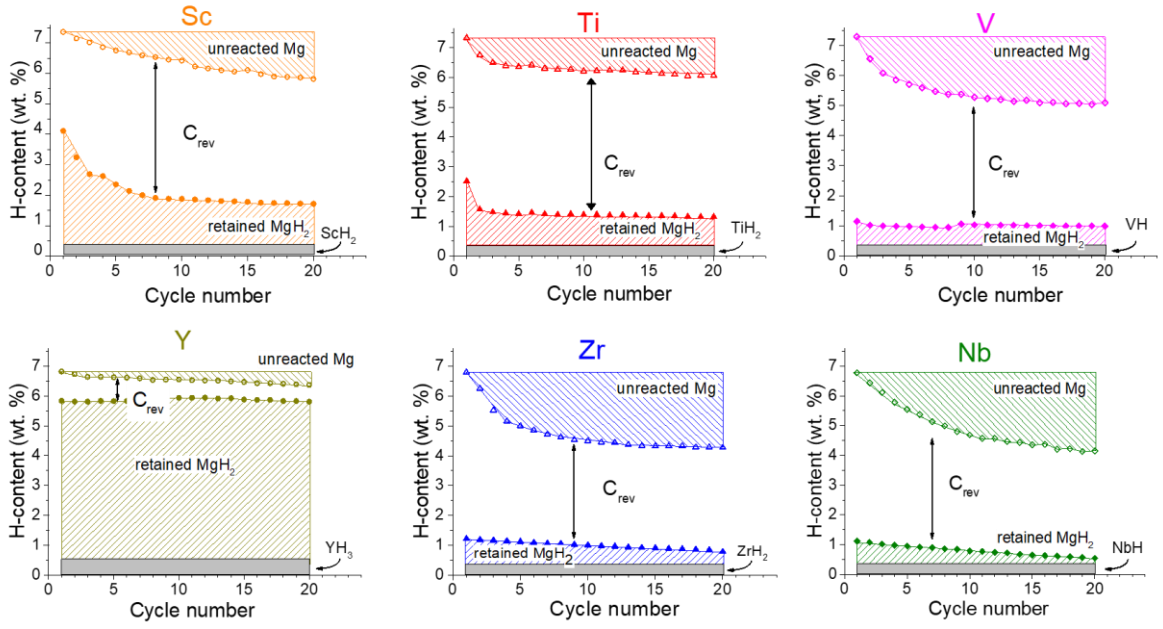

Figure 7. H-content in MgH_2-*ETM*H_x nanocomposites for subsequent desorption (full symbols) and absorption (empty symbols) sweeps. Hatched areas stand for retained MgH_2 and unreacted Mg at each sorption sweep, respectively. Hydrogen stored in *ETM*H*x* hydrides is displayed in grey at the bottom. The white area located between the upper and lower hatched ones gives the reversible capacity C_{rev}

The evolution of H-content in the Y-containing nanocomposite clearly differs from other NCs. The amount of retained MgH_2 is dramatically high from the first desorption sweep and remains practically unchanged on cycling. Indeed, the H-desorption kinetics of MgH_2-YH_3 nanocomposite is almost as sluggish as that of RBM MgH_2 (Fig. 5). Such a slow kinetics concurs with the lack of influence of YH_3 in the formation kinetics of MgH_2 by RBM (Fig. 1) pointing to the fact that the efficiency of YH_3 to transport hydrogen from the gas phase to Mg and from MgH_2 to the gas phase is very low. This cannot be attributed to sluggish diffusivity of hydrogen in yttrium hydrides. As a matter of fact, yttrium films used in switchable mirrors (which are based on the metal to semiconductor phase transition between YH_2 and YH_3) exhibit fast H-uptake even at room temperature [57]. Therefore, poor H-transport at YH_3 surface or YH_3/MgH_2 interfaces should be at the origin of sluggish kinetics in MgH_2-YH_3 nanocomposite. As concerns surface reactions, the electronic structure of the host metal is of paramount importance to dissociate or recombine hydrogen molecules at metal surfaces with low energy barrier [58]. Indeed, whereas H_2-surface reactions are difficult on Mg, early and late transition metals (characterized by empty and filled *d*-bands, respectively) are good surface catalysts [6,59,60]. The Fermi level of early and late transition metals is thus located around *s*-type orbitals, which is a necessary condition to promote H_2 surface reactions [58]. In contrast, MgH_2 and YH_3 hydrides, being both semiconductors with no available electronic states at the Fermi level [61], have little catalytic activity towards H_2 surface reactions. Indeed, in switchable mirrors this issue is overcome by covering yttrium films with a Pd overlayer that ensures H_2 dissociation and recombination [62]. Thus, we propose that both additive-free RBM MgH_2 and MgH_2-YH_3 nanocomposites exhibit sluggish desorption kinetics as result of poor recombination of hydrogen atoms into molecules at the surface.

Metallic hydrides from other early transition metals (ScH_2, TiH_2, ZrH_2, VH and NbH) are characterized by partially occupied *d*-bands near the Fermi level [63,64] that facilitate H_2-surface reactions. For instance, it has been experimentally demonstrated that $TiH_{1.95}$ hydride can easily dissociate and recombine hydrogen molecules at room temperature [65]. In this work, their use as additives clearly enhances the H-desorption rate of MgH_2 from the first cycle (Fig. 5) and leads to minor MgH_2 retention on cycling (Fig. 7). One may however argue that this improvement is less effective for Sc-additive which has moderate desorption kinetics (Fig. 5) and keeps significant amount of retained MgH_2 on cycling (Fig. 7). In addition, MgH_2-ScH_2 has a unique activation behaviour on cycling (Fig. 6). The peculiar H-properties of MgH_2-ScH_2 NC can be assigned to the singular conditions of MgH_2-ScH_2 synthesis for which scandium hydride, and not scandium metal, was used as RBM reactant. As a matter of fact, the crystallite size of this hydride (L ~ 30 nm) after RBM is much larger for Sc than for the other *ETM*H*x* additives. This suggests that crystallite size as well as the nature of MgH_2/*ETM*H*x* interfaces depend on the nanocomposite preparation route and influence its hydrogenation kinetics.

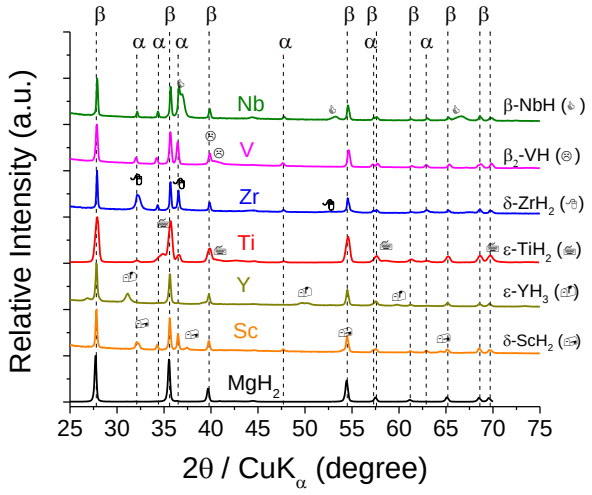

Figure 8. XRD patterns of 95MgH_2+*ETM*H_x nanocomposites after the 20th absorption sweep. Diffraction peaks from α-Mg and β-MgH_2 phases are marked by vertical lines. Diffraction peaks of *ETM*H_x phases are marked by symbols.

Let's focus now on the H-properties of *ETM*s belonging to groups 4 (Ti and Zr) and 5 (V and Nb). All related MgH_2-*ETM*H_x nanocomposites exhibit very fast desorption kinetics (Fig. 5), C_{rev} being limited by absorption ones. Absorption kinetics are characterized by a two-step reaction process, which is commonly attributed to fast and multiple formation of MgH_2 nuclei at defects (first stage) that grow and build-up a MgH_2 layer through which hydrogen diffusion [53,66] is very slow (second stage). As shown in Fig. 5, the kinetics of the second stage slows down on cycling, especially for Zr, V and Nb. Consequently, the amount of unreacted Mg gradually increases on cycling (Fig. 7) and the reversible hydrogen capacities steadily decrease (Fig. 6). One may hypothesize that slowing down of absorption kinetics is due to the enlargement of the MgH_2 layer as result of significant crystallite growth upon hydrogen absorption and desorption.

To verify this hypothesis, X-ray diffraction analysis have been performed on cycled samples after the 20th absorption sweep. XRD patterns are shown in Figure 8, the graphical output of Rietveld analysis is given in Figure S2 (ESI) and obtained crystallographic data are gathered in Table 3. As compared to the XRD patterns of as-synthetized NCs (Figure 2), main changes upon cycling concern the disappearance of γ-MgH_2 phase -a fact widely reported in literature-[50,53], the formation of α-Mg and the sharpening of β-MgH_2 diffraction peaks. Structural properties of *ETM*H_x hydrides are not significantly affected by H-cycling. They behave as catalysts. Ti-containing NC exhibits the largest broadening for β-MgH_2 diffraction peaks. Indeed, for Ti-containing NC crystallite size of β-MgH_2 remains small after cycling, L_{MgH2} = 24 ± 2 nm, whereas

it increases quite significantly for other *ETM*s such as Nb (L_{MgH2} = 100 ± 10 nm) and Zr (L_{MgH2} = 160 ± 20 nm). For Y-containing and additive-free samples, which hardly desorb hydrogen, the crystal size only enlarges moderately (L_{MgH2} ~50 nm) suggesting that crystal growth occurs preferentially after MgH_2 decomposition, *i.e.* in the Mg phase. It should be noted that the amount of unreacted Mg is high (above 20 wt.%), for *ETM* = Sc, Zr, V and Nb, whereas it is low, 7 ± 1 wt.%, for Ti-containing NC. Unreacted Mg amount concurs with H-content analysis in the NCs (Figure 7).

Table 3. Crystallographic data for 95MgH_2-5*ETM*H_x RBM nanocomposites after the 20th absorption sweep. Detected phases, space group (S.G.), cell parameters, crystallite size (*L*) and Rietveld relaibility factors (R_B, R_{wp}) are given. Standard deviations referring to the last digit are given in parenthesis.

Additive	Phase	Content (wt.%)	S.G.	Cell parameters			*L* (nm)	R_B (%)	R_{wp} (%)
				a (Å)	*b* (Å)	*c* (Å)			
Sc	δ-ScH_2	10(1)	*Fm-3m*	4.791(1)	-	-		2.8	3.1
	β-MgH_2	69(2)	*P*4_2/*mnm*	4.521(1)	-	3.024(1)	82(7)	3.5	
	Mg		*P*6_3/*mmc*	3.213(1)	-	5.217(1)	83(11)	2.8	
Y	ε-YH_3	14(1)	*P*-3*c*1	6.355(1)	-	6.611(1)	13(1)	3.5	3.1
	β-MgH_2	85(1)	*P*4_2/*mnm*	4.520(1)	-	3.023(1)	54(2)	1.9	
	Mg	1(1)	*P*6_3/*mmc*	3.210*	-	5.215*	54*	19	
Ti	ε-TiH_2	9(1)	*I4/mmm*	3.166(2)	-	4.407(4)	9(3)	12.6	20
	β-MgH_2	84(2)	*P*4_2/*mnm*	4.521(1)	-	3.024(1)	24(2)	5.5	
	Mg		*P*6_3/*mmc*	3.213(1)	-	5.215(3)	24(3)	25	
Zr	ε-ZrH_2	18(1)	*I4/mmm*	3.479(1)	-	4.575(1)	11(1)	7.8	5
	β-MgH_2	61(1)	*P*4_2/*mnm*	4.519(1)	-	3.022(1)	160(20)	4.8	
	Mg		*P*6_3/*mmc*	3.214(1)	-	5.220(1)	240(50)	7.4	
V	β_2-VH	8(1)	*I4/mmm*	3.119(1)	-	3.186(2)	7(2)	2.7	3.3
	β-MgH_2	65(1)	*P*4_2/*mnm*	4.504(1)	-	3.014(1)	52(2)	0.9	
	Mg		*P*6_3/*mmc*	3.212(1)	-	5.215(1)	56(5)	2.4	
Nb	β-NbH	17(1)	*Pnnn*	3.433(1)	4.905(1)	4.844(1)	17(2)	1.4	3.9
	β-MgH_2	58(1)	*P*4_2/*mnm*	4.519(1)	-	3.022(1)	100(10)	5.3	
	Mg		*P*6_3/*mmc*	3.211(1)	-	5.215(1)	103(15)	6.9	
No additive	β-MgH_2	99(1)	*P*4_2/*mnm*	4.520(1)	-	3.023(1)	49(1)	6.1	13
	Mg	1(1)	*P*6_3/*mmc*	3.210*	-	5.215*	49*	24	

* Values were fixed to ensure refinement convergence.

Figure 9 shows the extent of the Mg to MgH_2 reacted fraction, *F* (in %), for MgH_2-*ETM*H*x* nanocomposites at the 20th absorption sweep as a function of the MgH_2 crystal size L_{MgH2}, both *F* and L_{MgH2} being obtained from the Rietveld analysis of XRD data. As a general trend, it is clearly observed that the lower the crystal size, the higher the reacted fraction. It confirms that Ti-additive is the most efficient *ETM* to minimize MgH_2 crystal growth and thereby it keeps fast absorption kinetics on cycling and maximize the extent of the Mg to MgH_2 phase transformation. The fact that TiH_2 is the best grain growth inhibitor can be tentatively attributed to coherent coupling between Mg and TiH_2 thanks to their close molar volume, V_m = 13.8 and 13.2 cm^3, respectively [50,54,67]. Molar volume of all *ETM*H_x hydrides here studied and their comparison with those of Mg and MgH_2 are given in Table S1 (ESI).

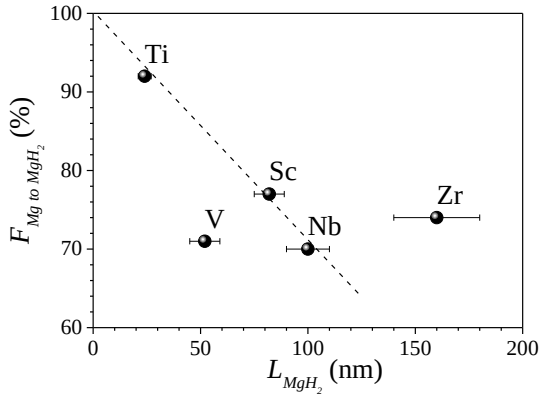

Figure 9. Dependence of the Mg to MgH_2 reacted fraction, *F*, on the MgH_2 crystallite size L_{MgH_2} for MgH_2-*ETM*H_x nanocomposites at the 20th absorption sweep. The dashed line is a guide to the eye.

A more critical analysis of Fig. 9 shows that some additives deviate from a linear correlation between *F* and L_{MgH2} suggesting that besides crystal size other factors play a role on the extent of the Mg to MgH_2 reaction *F*. Indeed, *F* is higher than expected for Zr-additive, whereas is lower for V-one. This scales with the relative difference in molar volume between the nucleating MgH_2 phase and *ETM*H_x hydrides $\Delta V_m/V_{m,MgH2}$ (Table S1). This difference is the lowest for Zr-additive, 11%, while it is the highest for V, 93%. Then, it can be reasonably proposed that MgH_2 preferentially nucleates at *ETM*H_x/Mg interfaces and that the energy barrier for nucleation decreases by lowering the molar volume difference between the nucleating MgH_2 phase and *ETM*H_x hydrides. Thus, MgH_2 nucleation energy barrier is much lower for Zr than for V. This observation also concurs with the fact that kinetics of MgH_2 formation by RBM (Fig. 1) is the fastest for Zr and the slowest for V (excluding the peculiar case of Y which suffers from additional surface barriers).

Conclusions

Reactive ball milling under hydrogen gas is an efficient method for the synthesis of nanostructured MgH_2 powders intimately mixed with hydrides of early transition metals of groups 3 to 5. MgH_2-*ETM*H_x nanocomposites consist of ~ 2 µm in size agglomerates formed by primary crystallite particles of ~20 nm in size. The H-thermodynamics of the Mg-H system are not significantly affected by the presence of *ETMH*$_x$ as no ternary Mg-*ETM*-H phases are formed and phase domains are too large to induce size-effects. In contrast, all studied *ETM*H_x but YH_3 strongly enhance hydrogen absorption and desorption kinetics of the Mg-H system.

The role of *ETM*Hx as catalysts of H-kinetics in Mg has been elucidated from conjoint analysis of H-sorption curves, evolution of H-content on cycling, and structural data. It is schematically depicted in Figure 10 for the absorption case. Compared to Mg metal, dissociation of molecular hydrogen into H-atoms (step 1) is favored by the presence of *ETM*H_x hydrides thanks to the availability of *s*-type orbitals around the Fermi level. Note that this also applies for the reversible reaction, *i.e.* H_2 recombination. Next, hydrogen atoms can diffuse extremely fast in *ETMH*$_x$ hydrides (step 2), having a diffusion coefficient five orders of magnitude higher than in MgH_2 [10,68,69]. Thus, H-atoms are quickly transferred to the *ETM*H_x/Mg interface where MgH_2 easy nucleates when a suitable lattice mismatch exists between the molar volumes of *ETM*H_x and MgH_2 phases (step 3). Moreover, structural coupling at *ETM*H_x/Mg interfaces minimizes Mg grain growth on cycling and provides structural stability as well as reversible hydrogen uptake. This occurs particularly for TiH_2, with a molar volume almost identical to Mg. Consequently, TiH_2 offers the best hydrogenation properties in terms of reversible capacity and cycling stability of all *ETM*H_x here studied. Outstanding kinetic and cycling properties of MgH_2-TiH_2 nanocomposites have been highlighted in many recent reports [12,28,30,36,50,70–74]. At the operation conditions used in the present study, a stable reversible capacity of 4.8 wt.% over 20 cycles is obtained for reaction time limited to 15 min. Further studies will be necessary for a deep characterization of MgH_2/*ETM*H_x interfaces as well as for long-term cycling (over hundreds to thousands of cycles) of these nanocomposite materials. The use of high-resolution techniques and spectroscopic methods for fine microstructural analysis, particularly of interfaces, will be required for this task. Previous works demonstrate that Transmission Electron Microscopy and neutron diffraction analysis are of particular interest for microstructural characterization [50,75], while MAS ^{2}H Nuclear Magnetic Resonance is well-suited to characterize hydrogen mobility and lattice coupling at MgH_2/*ETM*H_x interfaces [76,77]. Moreover, severe microstructural modifications, including migration of *ETM*H_x catalysts, may occur upon long-term cycling, which can be properly characterized by conjoint X-Ray Photoelectron Spectrometry and Microscopy studies [50,75,78]

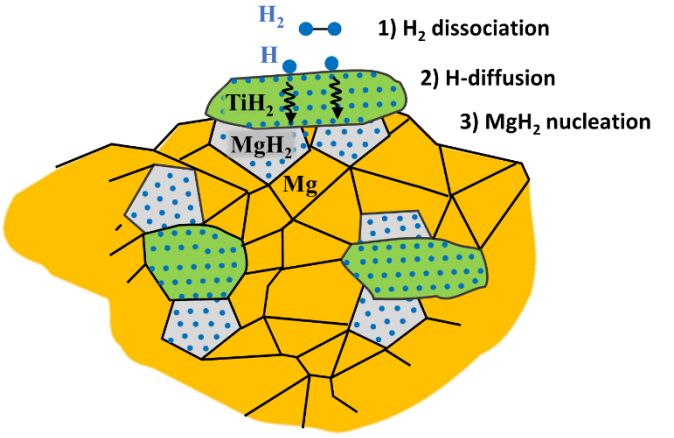

Figure 10. Schematic representation of a Mg-TiH_2 nanocomposite showing the role of TiH_2 (in green) to enhance hydrogen sorption kinetics in Mg (orange). TiH_2 helps to 1) dissociate H_2 molecules (in blue), 2) to transfer H atoms to the TiH_2/Mg interface and 3) to facilitate MgH_2 (in grey) nucleation.

Conflicts of interest

There are no conflicts to declare.

Acknowledgements

Dr. Pavel Rizo-Acosta thanks the Mexican government for his support through a SENER-CONACYT PhD grant. The authors are also grateful to Dr. Jean-Claude Crivello (ICMPE/CNRS) for his critical reading of the manuscript.

References

1 R. Weast, M. Astle and W. Beyer, in *CRC handbook of chemistry and physics: A ready-reference book of chemical and physical data*, Boca Raton, Fla: CRC Press, 1984.
2 K.-F. Aguey-Zinsou and J.-R. Ares-Fernández, *Energy Environ. Sci.*, 2010, **3**, 526.
3 J.-C. Crivello, B. Dam, R. V. Denys, M. Dornheim, D. M. Grant, J. Huot, T. R. Jensen, P. de Jongh, M. Latroche, C. Milanese, D. Milčius, G. S. Walker, C. J. Webb, C. Zlotea and V. A. Yartys, *Appl. Phys. A*, 2016, **122**, 97.
4 A. San-Martin and F. D. Manchester, *J. Phase Equilibria*, 1987, **8**, 431–437.
5 B. Vigeholm, K. Jensen, B. Larsen and A. Schrøder-Pedersen, *J. Common Met.*, 1987, **131**, 133–141.
6 T. Vegge, *Phys. Rev. B*, 2004, **70**, 035412.
7 O. Friedrichs, J. C. Sánchez-López, C. López-Cartes, M. Dornheim, T. Klassen, R. Bormann and A. Fernández, *Appl. Surf. Sci.*, 2006, **252**, 2334–2345.
8 N. Gérard and S. Ono, in *Topics in Applied Physics*, ed. L. Schlapbach, Springer-Verlag, New York, 1992, vol. 67, pp. 178–182.
9 J. F. Fernández and C. R. Sánchez, *J. Alloys Compd.*, 2002, **340**, 189–198.
10 X. Yao, Z. H. Zhu, H. M. Cheng and G. Q. Lu, *J. Mater. Res.*, 2008, **23**, 336–340.
11 F. Leardini, J. R. Ares, J. F. Fernández, J. Bodega and C. Sánchez, *Int. J. Hydrog. Energy*, 2011, **36**, 8351–8357.
12 G. Liang, J. Huot, S. Boily, A. Van Neste and R. Schulz, *J. Alloys Compd.*, 1999, **292**, 247–252.
13 G. Barkhordarian, T. Klassen and R. Bormann, *Scr. Mater.*, 2003, **49**, 213–217.
14 C. J. Webb, *J. Phys. Chem. Solids*, 2015, **84**, 96–106.
15 F. Tonus, V. Fuster, G. Urretavizcaya, F. J. Castro and J.-L. Bobet, *Int. J. Hydrog. Energy*, 2009, **34**, 3404–3409.
16 D. Chen, Y. M. Wang, L. Chen, S. Liu, C. X. Ma and L. B. Wang, *Acta Mater.*, 2004, **52**, 521–528.
17 B. R. Pauw, W. P. Kalisvaart, S. X. Tao, M. T. M. Koper, A. P. J. Jansen and P. H. L. Notten, *Acta Mater.*, 2008, **56**, 2948–2954.
18 F. Cuevas, J.-F. Fernández, J. R. Ares, F. Leardini and M. Latroche, *J. Solid State Chem.*, 2009, **182**, 2890–2896.
19 J. F. Fernandez, J. R. Ares, F. Cuevas, J. Bodega, F. Leardini and C. Sánchez, *Intermetallics*, 2010, **18**, 233–241.
20 K. Alsabawi, T. A. Webb, E. MacA. Gray and C. J. Webb, *Int. J. Hydrog. Energy*, 2017, **42**, 5227–5234.
21 J. Huot, D. B. Ravnsbæk, J. Zhang, F. Cuevas, M. Latroche and T. R. Jensen, *Prog. Mater. Sci.*, 2013, **58**, 30–75.
22 R. W. P. Wagemans, J. H. van Lenthe, P. E. de Jongh, A. J. van Dillen and K. P. de Jong, *J. Am. Chem. Soc.*, 2005, **127**, 16675–16680.
23 P. E. de Jongh and P. Adelhelm, *ChemSusChem*, 2010, **3**, 1332–1348.
24 J.-L. Bobet, E. Akiba, Y. Nakamura and B. Darriet, *Int. J. Hydrog. Energy*, 2000, **25**, 987–996.
25 G. Liang, J. Huot, S. Boily, A. Van Neste and R. Schulz, *J. Alloys Compd.*, 1999, **2991**, 295–299.
26 J. R. Ares, F. Cuevas and A. Percheron-Guégan, *Acta Mater.*, 2005, **53**, 2157–2167.
27 F. D. Manchester, *Phase Diagrams of Binary Hydrogen Alloys*, ASM International, Materials Park, OH, 2000.
28 F. Cuevas, D. Korablov and M. Latroche, *Phys. Chem. Chem. Phys.*, 2012, **14**, 1200–1211.
29 X. Luo, D. M. Grant and G. S. Walker, *J. Alloys Compd.*, 2015, **622**, 842–850.
30 N. Patelli, M. Calizzi, A. Migliori, V. Morandi and L. Pasquini, *J. Phys. Chem. C*, 2017, **121**, 11166–11177.
31 A. Zaluska, L. Zaluski and J. O. Ström–Olsen, *J. Alloys Compd.*, 1999, **288**, 217–225.
32 J. Huot, J. F. Pelletier, L. B. Lurio, M. Sutton and R. Schulz, *J. Alloys Compd.*, 2003, **348**, 319–324.
33 C. Ren, Z. Z. Fang, C. Zhou, J. Lu, Y. Ren and X. Zhang, *J. Phys. Chem. C*, 2014, **118**, 21778–21784.
34 G. Liang, J. Huot, S. Boily and R. Schulz, *J. Alloys Compd.*, 2000, **305**, 239–245.
35 A. R. Yavari, J. F. R. de Castro, G. Vaughan and G. Heunen, *J. Alloys Compd.*, 2003, **353**, 246–251.
36 P. Rizo-Acosta, F. Cuevas and M. Latroche, *Int. J. Hydrog. Energy*, 2018, **43**, 16774–16781.
37 M. Dornheim, S. Doppiu, G. Barkhordarian, U. Boesenberg, T. Klassen, O. Gutfleisch and R. Bormann, *Scr. Mater.*, 2007, **56**, 841–846.
38 J. Zhang, F. Cuevas, W. Zaïdi, J.-P. Bonnet, L. Aymard, J.-L. Bobet and M. Latroche, *J. Phys. Chem. C*, 2011, **115**, 4971–4979.
39 J. Rodriguez-Carvajal, *Phys. B*, 1993, **192**, 55–69.
40 H. M. Rietveld, *J. Appl. Crystallogr.*, 1969, **2**, 65–71.
41 B. O. Loopstra and H. M. Rietveld, *Acta Crystallogr. Sect. B*, 1969, **25**, 787–791.
42 T. P. Blach and E. MacA. Gray, *J. Alloys Compd.*, 2007, **446–447**, 692–697.
43 B. Bogdanovic, K. Bohmhammel, B. Christ, A. Reiser, K. Schlichte, R. Vehlen and U. Wolf, *J. Alloys Compd.*, 1999, **282**, 84–92.
44 M. V. Lototskyy, M. W. Davids, I. Tolj, Y. V. Klochko, B. S. Sekhar, S. Chidziva, F. Smith, D. Swanepoel and B. G. Pollet, *Int. J. Hydrog. Energy*, 2015, **40**, 11491–11497.
45 M. Bortz, B. Bertheville, G. Böttger and K. Yvon, *J. Alloys Compd.*, 20101120, **287**, L4–L6.
46 S. Orimo, F. Kimmerle and G. Majer, *Phys. Rev. B*, 2001, **63**, 94307–93316.
47 H. Müller and K. Weymann, *J. -Common Met.*, 1986, **119**, 115–126.
48 J. J. Reilly and R. H. Wiswall, *Inorg. Chem.*, 1970, **9**, 1678–1682.
49 N. Berti, F. Cuevas, J. Zhang and M. Latroche, *Int. J. Hydrog. Energy*, 2017, **42**, 22615–22621.
50 M. Ponthieu, F. Cuevas, J. F. Fernández, L. Laversenne, F. Porcher and M. Latroche, *J. Phys. Chem. C*, 2013, **117**, 18851–18862.
51 L. N. Yannopoulos, R. K. Edwards and P. G. Wahlbeck, *J. Phys. Chem.*, 1965, **69**, 2510–2515.

52 A. Khawam and D. R. Flanagan, *J. Phys. Chem. B*, 2006, **110**, 17315–17328.
53 R. A. Varin, T. Czujko and Z. Wronski, *Nanomaterials for solid state hydrogen storage*, Springer, Cleveland, 2009.
54 S. Hao and D. S. Sholl, *J. Phys. Chem. C*, 2012, **116**, 2045–2050.
55 V. A. Yartys, M. V. Lototskyy, E. Akiba, R. Albert, V. E. Antonov, J. R. Ares, M. Baricco, N. Bourgeois, C. E. Buckley, J. M. Bellosta von Colbe, J.-C. Crivello, F. Cuevas, R. V. Denys, M. Dornheim, M. Felderhoff, D. M. Grant, B. C. Hauback, T. D. Humphries, I. Jacob, T. R. Jensen, P. E. de Jongh, J.-M. Joubert, M. A. Kuzovnikov, M. Latroche, M. Paskevicius, L. Pasquini, L. Popilevsky, V. M. Skripnyuk, E. Rabkin, M. V. Sofianos, A. Stuart, G. Walker, H. Wang, C. J. Webb and M. Zhu, *Int. J. Hydrog. Energy*, 2019, **44**, 7809–7859.
56 J. J. Reilly and R. H. Wiswall, *Inorg. Chem.*, 1968, **7**, 2254–2256.
57 J. N. Huiberts, R. Griessen, J. H. Rector, R. J. Wijngaarden, J. P. Dekker, D. G. de Groot and N. J. Koeman, *Nature*, 1996, **380**, 231–234.
58 J. Harris, *Appl. Phys. A*, 1988, **47**, 63–71.
59 L. Schlapbach, in *Hydrogen in Intermetallic Compunds II*, Springer-Verlag, Berlin, 1992, pp. 15–95.
60 A. Züttel, M. Hirscher, B. Panella, K. Yvon, S. Orimo, B. Bogdanović, M. Felderhoff, F. Schüth, A. Borgschulte, S. Goetze, S. Suda and M. T. Kelly, in *Hydrogen as a Future Energy Carrier*, eds. A. Züttel, A. Borgschulte and L. Schlapbach, Wiley-VCH Verlag GmbH & Co. KGaA, 2008, pp. 165–263.
61 Z. Wu, R. E. Cohen, D. J. Singh, R. Gupta and M. Gupta, *Phys. Rev. B*, 2004, **69**, 085104.
62 J. N. Huiberts, J. H. Rector, R. J. Wijngaarden, S. Jetten, D. De Groot, B. Dam, N. J. Koeman, R. Griessen, B. Hjörvarsson and S. Olafsson, *J. Alloys Compd.*, 1996, **239**, 158–171.
63 J. H. Weaver, D. J. Peterman, D. T. Peterson and A. Franciosi, *Phys. Rev. B*, 1981, **23**, 1692.
64 J. H. Weaver and D. T. Peterson, *J. Common Met.*, 1980, **74**, 207–216.
65 E. Nowicka and R. Duś, *Langmuir*, 1996, **12**, 1520–1527.
66 G. Friedlmeier and M. Groll, *J. Alloys Compd.*, 1997, **253–254**, 550–555.
67 D. M. Borsa, R. Gremaud, A. Baldi, H. Schreuders, J. H. Rector, B. Kooi, P. Vermeulen, P. H. L. Notten, B. Dam and R. Griessen, *Phys. Rev. B*, 2007, **75**, 205408–9.
68 U. Kaess, G. Majer, M. Stoll, D. T. Peterson and R. G. Barnes, *J. Alloys Compd.*, 1997, **259**, 74–82.
69 S. Hao and D. S. Sholl, *Appl. Phys. Lett.*, 2008, **93**, 251901.
70 J. Lu, Y. J. Choi, Z. Z. Fang, H. Y. Sohn, E. Rönnebro and E. H. Majzoub, *J. Am. Chem. Soc.*, 2009, **131**, 15843–15852.
71 J. Lu, Y. J. Choi, Z. Z. Fang, H. Y. Sohn and E. Rönnebro, *J. Am. Chem. Soc.*, 2010, **132**, 6616–6617.
72 T. Liu, C. Chen, F. Wang and X. Li, *J. Power Sources*, 2014, **267**, 69–77.
73 C. Zhou, Z. Z. Fang and R. C. Bowman, *J. Phys. Chem. C*, 2015, **119**, 22261–22271.
74 X. Ma, X. Xie, P. Liu, L. Xu and T. Liu, *Prog. Nat. Sci. Mater. Int.*, 2017, **27**, 99–104.
75 C. Zhou, Z. Z. Fang, R. C. Bowman, Y. Xia, J. Lu, X. Luo and Y. Ren, *J. Phys. Chem. C*, 2015, **119**, 22272–22280.
76 S. Srinivasan, P. C. M. M. Magusin, W. P. Kalisvaart, P. H. L. Notten, F. Cuevas, M. Latroche and R. A. van Santen, *Phys. Rev. B*, 2010, **81**, 054107.
77 K. Asano, H. Kim, K. Sakaki, K. Jimura, S. Hayashi, Y. Nakamura, K. Ikeda, T. Otomo, A. Machida and T. Watanuki, *Inorg. Chem.*, 2018, **57**, 11831–11838.
78 J. Cui, H. Wang, J. Liu, L. Ouyang, Q. Zhang, D. Sun, X. Yao and M. Zhu, *J. Mater. Chem. A*, 2013, **1**, 5603–5611.

